Seismological evidence for girdled olivine lattice-preferred orientation in oceanic lithosphere and implications for mantle deformation processes during seafloor spreading

J. B. Russell[1], J. B. Gaherty[2], H. F. Mark[3], G. Hirth[1], L. N. Hansen[4], D. Lizarralde[3], J. A. Collins[3], R. L. Evans[3]

[1]Department of Earth, Environmental and Planetary Sciences, Brown University, Providence, RI, USA.

[2]School of Earth and Sustainability, Northern Arizona University, Flagstaff, Arizona, USA.

[3]Woods Hole Oceanographic Institution, Woods Hole, MA, USA

[4]Department of Earth and Environmental Sciences, University of Minnesota, Minneapolis, MN, USA

Contents of this file

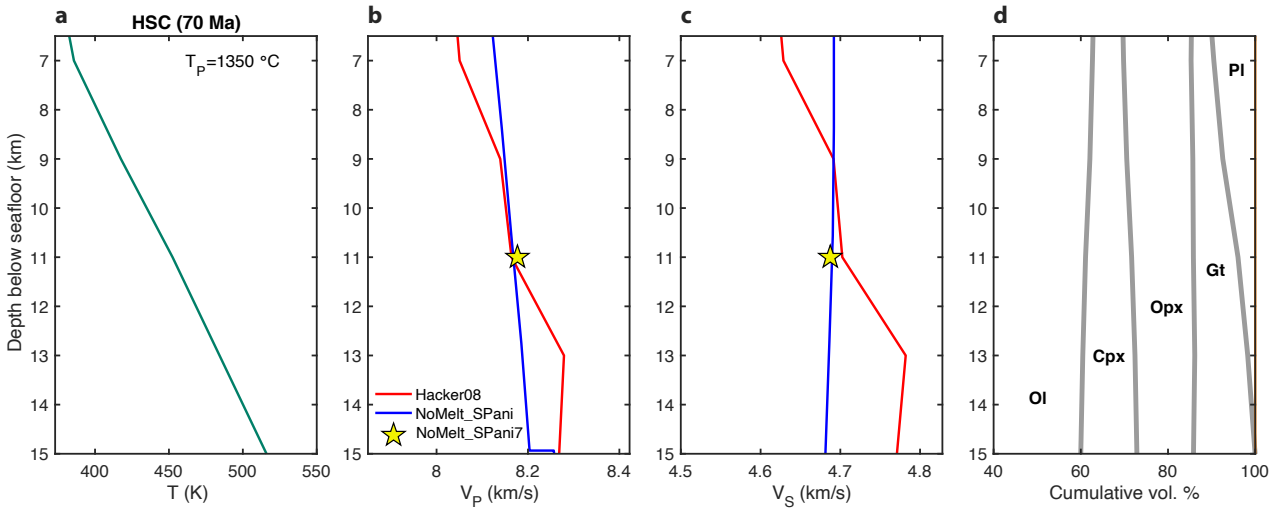

Figure S1. Estimating V_P, V_S, and olivine content. **a** 70 Ma half-space cooling (HSC) geotherm with mantle potential temperature $T_P = 1350°C$. **b, c** Mineral physics calculations of Voigt average V_P and V_S (red solid lines) and **d** mineral abundance from Perple_X (Connolly, 2009), using the solution models of Stixrude & Lithgow-Bertelloni (2011) and assuming a depleted mid-ocean ridge basalt (MORB) mantle composition (Hacker, 2008). The average velocities for the upper 7 km, NoMelt_SPani7, is indicated by the yellow star. Although the predicted velocity gradients are less steep for both V_P and V_S (and for V_P, opposite in sign), there is fair agreement with the depth averaged NoMelt velocities. Modal estimates yield ~60% olivine. Ol = olivine; Cpx = clinopyroxene; Opx = orthopyroxene; Gt = garnet; Pl = plagioclase

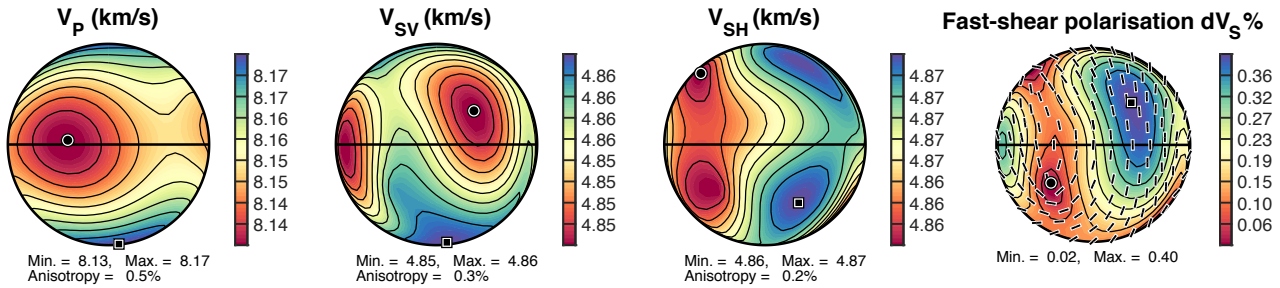

Figure S2. Orthopyroxene texture used in calculations. A generic orthopyroxene texture from the torsion experiments of Hansen et al. (2014). The fabric is extremely weak ($\sim$0.4% V_{P} anisotropy) and oriented with its [100] crystallographic axis perpendicular to the shear plane, [001] sub-parallel to the shear direction, and [010] perpendicular to shear and in the shear plane. $dV_{\mathrm{S}} = 200(V_{\mathrm{SH}} - V_{\mathrm{SV}})/(V_{\mathrm{SH}} + V_{\mathrm{SV}})$

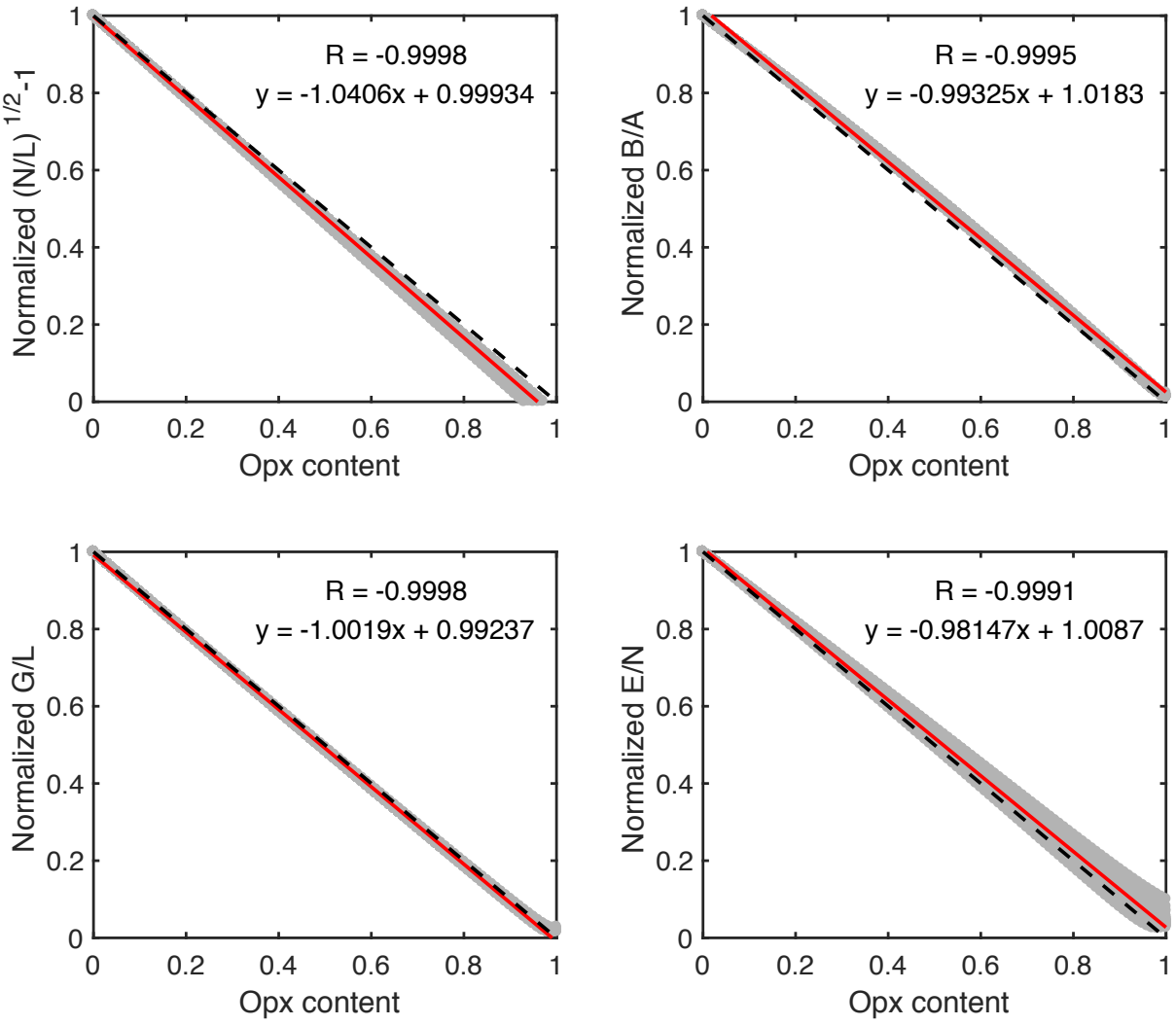

Figure S3. Reduction in anisotropy strength with increasing orthopyroxene content. Using well-developed laboratory olivine samples from Hansen et al. (2014, 2016) with shear strains of $\gamma > 2$, shown in grey, scaling relationships are found between orthopyroxene content and anisotropy strength (using the orthopyroxene fabric in Figure S2; see methods for details). Anisotropy values for each sample are normalized by the pure olivine estimate in order to determine a single scaling relation for all samples. The best fit line that describes anisotropy reduction with increasing orthopyroxene is shown in red, and nearly falls along the -1:1 line dashed in black.

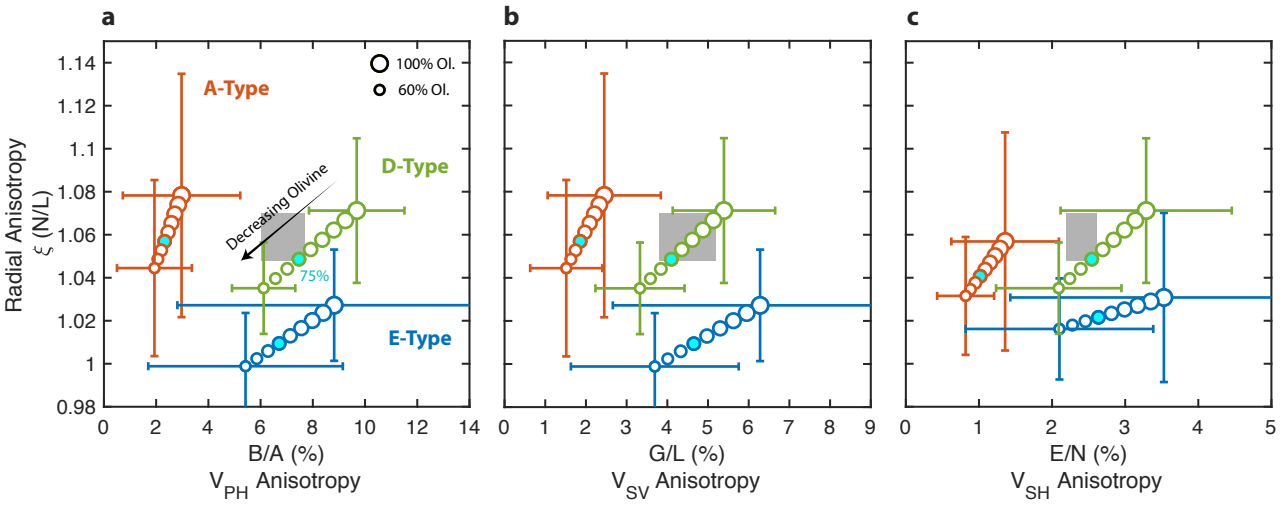

Figure S4. Effect of assumed olivine content on LPO-type comparison. a–c, As in Figure 5 in the main text. Circles show anisotropy averages assuming varying ratios of olivine and pyroxene content, where symbol size scales with the amount of olivine ranging from 60% to 100% in increments of 5%, and color denotes fabric type. Anisotropy strength decreases with decreasing olivine content. The best fitting composition of 75% olivine and 25% is shown in cyan.

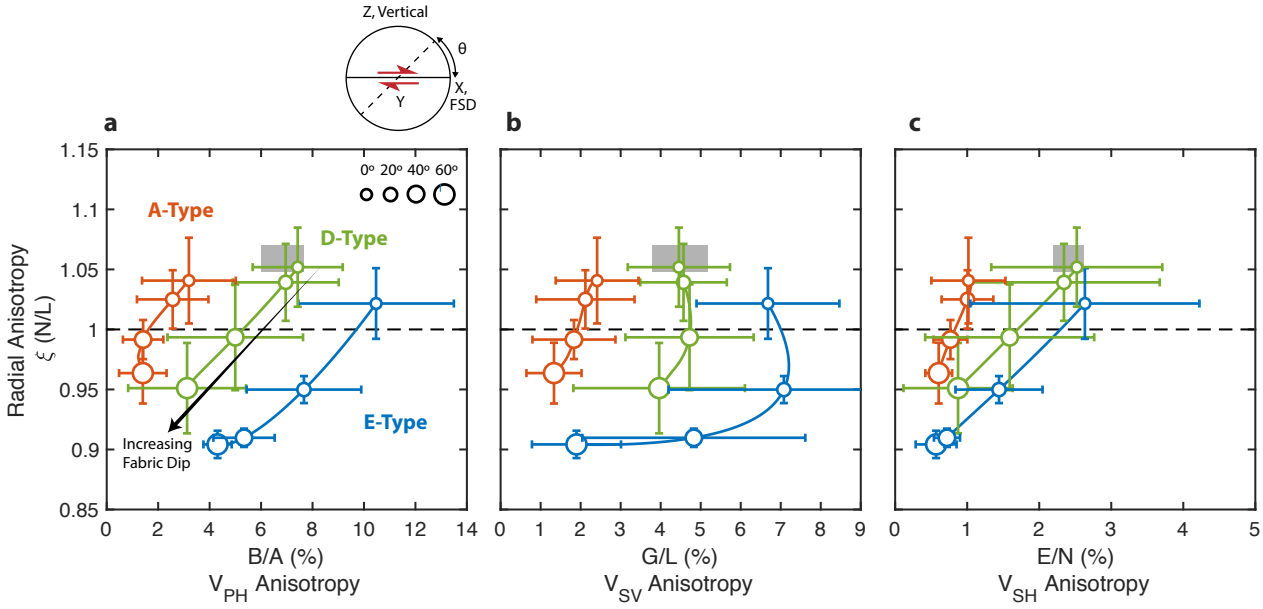

Figure S5. Effect of fabric dip on LPO-type comparison. a–c, As in Figure 5 in the main text. Symbols show anisotropy averages and one standard deviation after rotating samples about the Y axis by an angle θ, effectively rotating [100] out of the shear plane. Symbol size scales with introduced fabric dip ranging from 0° to 60°, and color denotes fabric type. A composition of 75% olivine and 25% orthopyroxene is assumed. Radial and azimuthal anisotropy generally decreases with increasing fabric dip. In detail, V_{SV} anisotropy in **b** shows a more complex behavior, in particular for samples with strong azimuthal anisotropy, where an initial slight increase with dip to 20-40° is followed by a nonlinear decrease.

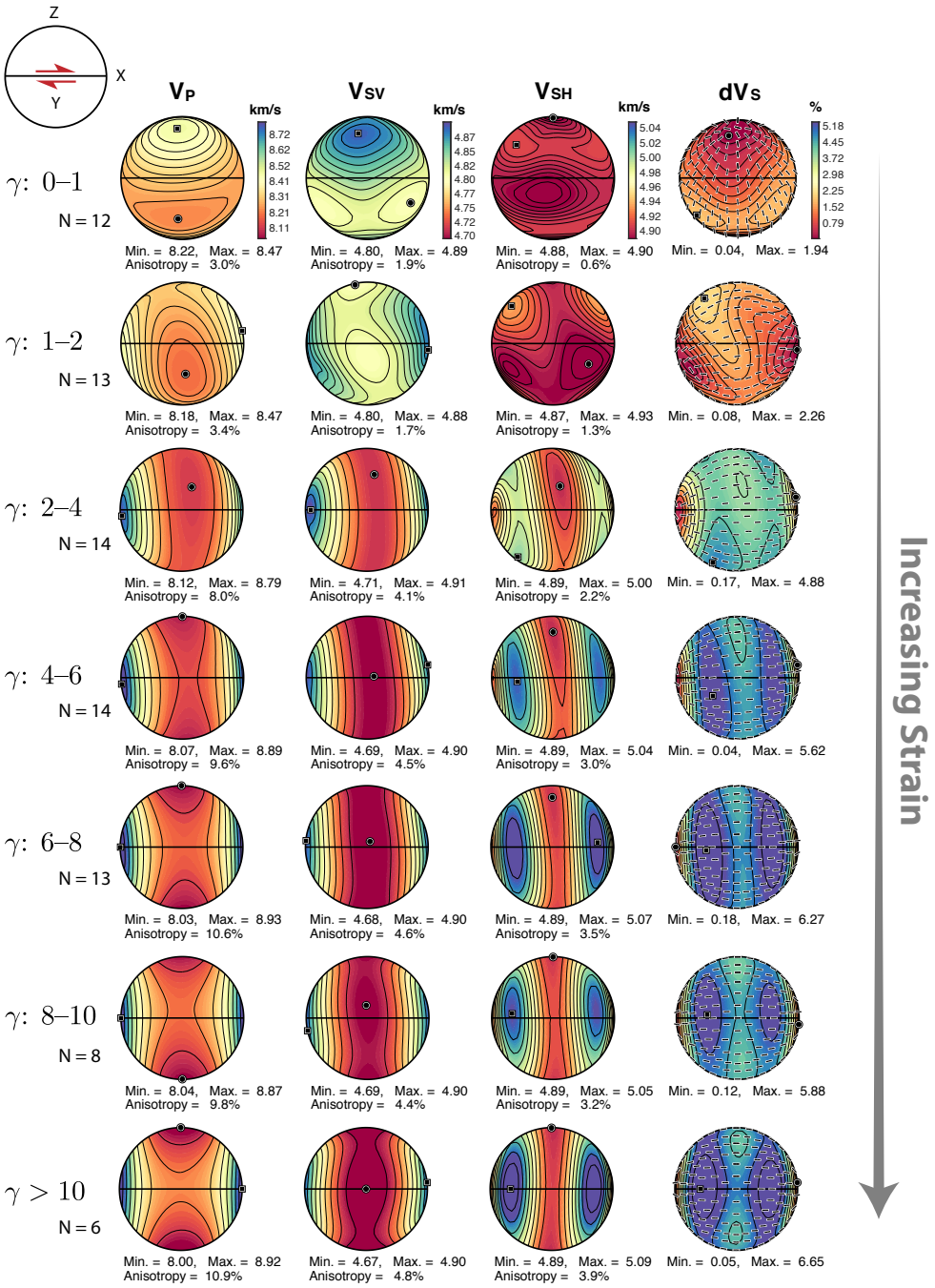

Figure S6. Strain evolution of anisotropy for laboratory samples shown in Figure 3. (left to right) Columns show V_{P}, V_{SV}, V_{SH}, and dV_{S} anisotropy for laboratory samples from Hansen et al. (2014, 2016) grouped and averaged by shear strain for 60% olivine and 40% pyroxene. (top to bottom) Each row represents an average of all samples within the range of γ indicated at the left of each row. Strain increases from top to bottom. A common color scale is used for each column. $dV_{\mathrm{S}} = 200(V_{\mathrm{SH}} - V_{\mathrm{SV}})/(V_{\mathrm{SH}} + V_{\mathrm{SV}})$

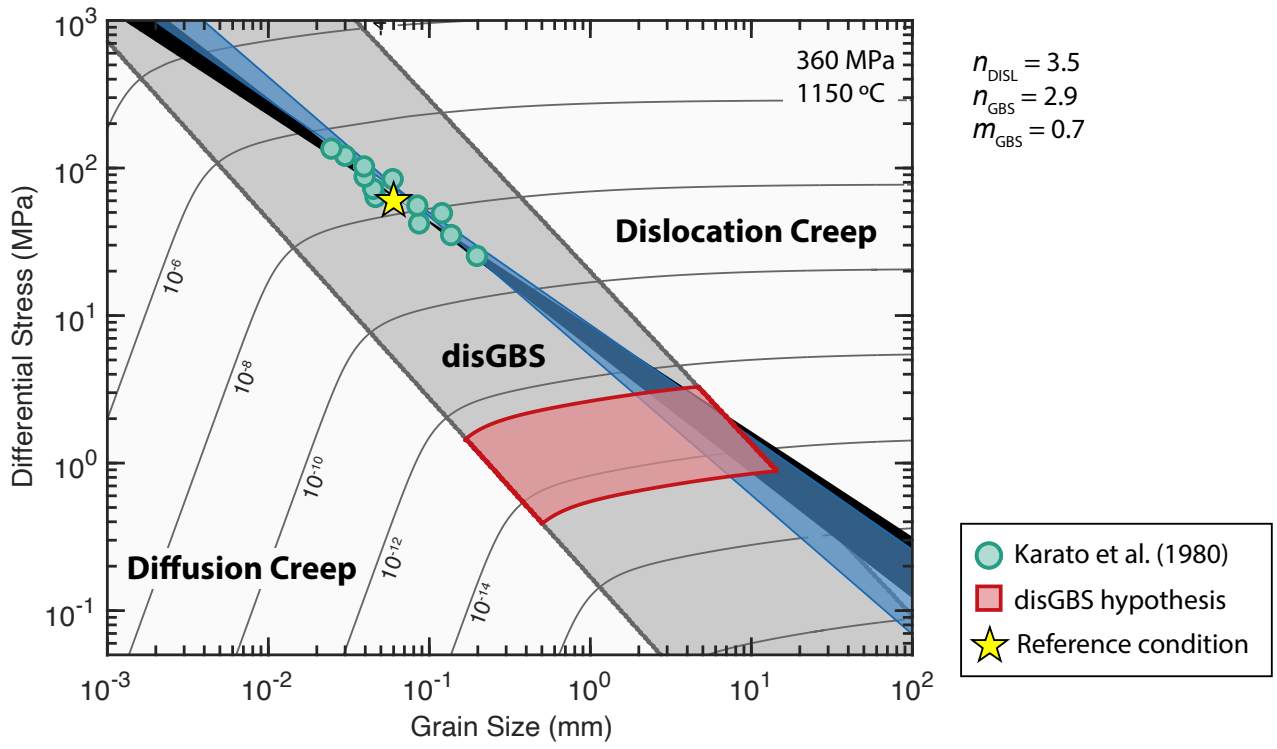

Figure S7. Deformation mechanism map for low temperature endmember. As in Figure 6 in the main text but for a temperature of 1150°C. Although it is possible that a small amount of strain did accumulate at ∼1150°C as the lithosphere cooled, it is likely that the majority of strain was accumulated at warmer conditions, and thus a temperature of ∼1250°C is more representative of the LPO we observe.

Table S1. NoMelt_SPani transversely isotropic velocity model with depth relative to sea surface.

Depth (km)	V_{SV} (km/s)	V_{SH} (km/s)	V_{PV} (km/s)	V_{PH} (km/s)	η	ρ (g cm^{-3})
0.000	0.000	0.000	1.500	1.500	1.00	1.030
5.225	0.000	0.000	1.500	1.500	1.00	1.030
5.225	0.150	0.150	1.900	1.900	1.00	1.500
5.375	0.150	0.150	1.900	1.900	1.00	1.500
5.375	3.046	3.046	5.635	5.635	1.00	3.027
7.750	3.699	3.828	6.844	7.082	1.00	3.027
8.626	3.783	3.915	6.999	7.242	1.00	3.027
10.300	3.842	3.976	7.108	7.355	1.00	3.027
11.610	3.906	4.042	7.227	7.478	1.00	3.027
11.610	4.646	4.783	7.934	8.168	0.90	3.339
13.600	4.646	4.783	7.955	8.189	0.90	3.340
15.790	4.644	4.781	7.975	8.210	0.90	3.341
17.980	4.640	4.777	7.997	8.232	0.90	3.342
20.160	4.635	4.772	8.014	8.250	0.90	3.343
20.160	4.635	4.772	8.066	8.303	0.90	3.343
23.870	4.627	4.764	8.119	8.358	0.91	3.346
25.725	4.623	4.760	8.146	8.385	0.91	3.347
27.580	4.619	4.755	8.171	8.412	0.91	3.349
29.435	4.614	4.751	8.198	8.439	0.91	3.350

Table S2. NoMelt_SPani azimuthal anisotropy model with depth relative to sea surface.

Depth (km)	G/L (%)	Ψ_{G} (°)	B/A (%)	Ψ_{B} (°)	E/N (%)	Ψ_{E} (°)	H/F (%)	Ψ_{H} (°)
13.600	4.25	75.69	6.28	83.35	2.38	124.61	0.47	165.53
15.790	4.56	76.93	6.85	83.34	2.39	124.41	0.50	166.72
17.980	4.86	77.90	7.38	83.17	2.40	124.07	0.53	167.70
20.160	5.27	78.80	8.01	82.18	2.42	123.29	0.58	168.67
23.870	5.61	78.90	8.46	80.50	2.46	122.25	0.62	168.79
25.725	5.73	78.74	8.62	79.73	2.48	121.75	0.63	168.67
27.580	5.83	78.45	8.76	78.92	2.51	121.18	0.64	168.41
29.435	5.90	78.06	8.85	78.23	2.53	120.67	0.65	168.04

Table S3. Nominal flow law and grain-size evolution parameters used to calculate the wattmeter and deformation mechanism maps

Symbol	Description	Value	Units
R	gas constant	8.314	J mol^{-1} K^{-1}
T	temperature	1523	K
P	pressure	360	MPa
G_0	dry grain growth rate constant	1.5×10^{-5}	m^p s^{-1}
E_g	activation energy for grain growth	350	kJ mol^{-1}
V_g	activation volume for grain growth	8×10^{-6}	m^3 mol^{-1}
p	grain growth exponent	3	
χ	fraction of work done by dislocation mechanisms	0.03	
γ	average specific grain boundary energy	1	J m^{-2}
c	geometric constant	3	
n_{GBS}	disGBS stress exponent	2.9	
m_{GBS}	disGBS grain-size exponent	0.7	
A_{GBS}	disGBS prefactor	$10^{4.8}$	μm$^{-0.7}$ MPa$^{-2.9}$ s^{-1}
E_{GBS}	disGBS activation energy	4.45×10^5	J mol^{-1}
V_{GBS}	disGBS activation volume	1.5×10^{-5}	m^3 mol^{-1}
n_{DISL}	dislocation creep stress exponent	3.5	
m_{DISL}	dislocation creep grain-size exponent	0	
A_{DISL}	dislocation creep prefactor	1.1×10^5	MPa$^{-3.5}$ s^{-1}
E_{DISL}	dislocation creep activation energy	5.3×10^5	J mol^{-1}
V_{DISL}	dislocation creep activation volume	1.5×10^{-5}	m^3 mol^{-1}
n_{DIFF}	diffusion creep stress exponent	1	
m_{DIFF}	diffusion creep grain-size exponent	3	
A_{DIFF}	diffusion creep prefactor	$10^{7.6}$	μm^{-3} MPa^{-1} s^{-1}
E_{DIFF}	diffusion creep activation energy	3.75×10^5	J mol^{-1}
V_{DIFF}	diffusion creep activation volume	1×10^{-5}	m^3 mol^{-1}

References

Connolly, J. A. (2009). The geodynamic equation of state: What and how. *Geochemistry, Geophysics, Geosystems*, *10*(10). doi: 10.1029/2009GC002540

Hacker, B. R. (2008). H2O subduction beyond arcs. *Geochemistry, Geophysics, Geosystems*, *9*(3). doi: 10.1029/2007GC001707

Hansen, L. N., Warren, J. M., Zimmerman, M. E., & Kohlstedt, D. L. (2016). Viscous anisotropy of textured olivine aggregates, Part 1: Measurement of the magnitude and evolution of anisotropy. *Earth and Planetary Science Letters*, *445*, 92–103. Retrieved from http://dx.doi.org/10.1016/j.epsl.2016.04.008 doi: 10.1016/j.epsl.2016.04.008

Hansen, L. N., Zhao, Y. H., Zimmerman, M. E., & Kohlstedt, D. L. (2014). Protracted fabric evolution in olivine: Implications for the relationship among strain, crystallographic fabric, and seismic anisotropy. *Earth and Planetary Science Letters*, *387*, 157–168. Retrieved from http://dx.doi.org/10.1016/j.epsl.2013.11.009 doi: 10.1016/j.epsl.2013.11.009

Stixrude, L., & Lithgow-Bertelloni, C. (2011). Thermodynamics of mantle minerals - II. Phase equilibria. *Geophysical Journal International*, *184*(3), 1180–1213. doi: 10.1111/j.1365-246X.2010.04890.x